Catalytic mechanism and design principle of coordinately unsaturated single metal atom-doped covalent triazine frameworks with high activity and selectivity for CO_2 electroreduction†

Lele Gong,[a] Xiaowei Wang,[b] Tao Zheng,[c] Jerry Liu,[b] Jie Wang,[b] Yu-Chia Yang,[b] Jing Zhang,[c] Xiao Han,[c] Lipeng Zhang *[a] and Zhenhai Xia *[b]

[a]College of Chemical Engineering, Beijing University of Chemical Technology, Beijing, 100029, China. E-mail: zhanglipeng2011@gmail.com

[b]Department of Materials Science and Engineering, University of North Texas, Denton, TX 76203, USA. E-mail: Zhenhai.xia@unt.edu

[c]School of Materials Science and Engineering, Northwestern Polytechnical University, Xi'an, 710072, China

Electrochemical conversion of carbon dioxide (CO_2) to chemicals or fuels can effectively promote carbon capture and utilization, and reduce greenhouse gas emission but a serious impediment to the process is to find highly active electrocatalysts that can selectively produce desired products. Herein, we have established the design principles based on the density functional theory calculations to screen the most promising catalysts from the family of coordinately unsaturated/saturated transition metal (TM) embedded into covalent organic frameworks (TM-COFs). An intrinsic descriptor has been discovered to correlate the molecular structures of the active centers with both the activity and selectivity of the catalysts. Among all the catalysts, the coordinately unsaturated Ni-doped covalent triazine framework (Ni-CTF) is identified as one of the best electrocatalysts with the lowest overpotential (0.34 V) for CO_2 reduction toward CO while inhibiting the formation of the side products, H_2 and formic acid. Compared with coordinately saturated TM-COFs and noble metals (*e.g.* Au and Ag), TM-CTFs exhibit higher catalytic activity and stronger inhibition of side products. The predictions are supported by previous experimental results. This study provides an effective strategy and predictive tool for developing desired catalysts with high activity and selectivity.

1 Introduction

Electrocatalytic carbon dioxide (CO_2) reduction is a promising strategy to reduce CO_2 in the atmosphere and produce carbon neutral fuels or industrial chemicals, which would alleviate the global greenhouse gas issues and enable sustainable development in energy economy and the chemical industry.[1–5] In the CO_2 reduction reaction (CO_2RR), carbon monoxide (CO) is one of the primary products when using catalysts such as iron, cobalt, and nickel-based materials.[6] In particular, their single-atom catalysts (SACs) have become popular in CO_2 conversion.[7–11] Due to the high chemical inertness of CO_2 molecules, however, there is a large energy barrier in the elementary reaction of $*CO_2$ chemisorption or CO desorption according to the first-principles calculation.[12,13] This will undoubtedly hinder the reaction rate and increase the overpotential for electrocatalytic reduction of CO_2 to CO. Moreover, the undesirable side-reaction, the hydrogen evolution reaction (HER), will also share the catalysts in aqueous electrolytes because of its similar equilibrium potentials to the CO_2RR.[14] Therefore, there is still an urgent desire to solve the problems of low efficiency and poor selectivity in the CO_2RR, as well as sluggish reaction kinetics. For this purpose, the development of highly effective electro- catalysts for the CO_2RR is becoming increasingly important.

Previous work has shown that the catalyst structures with coordinately unsaturated metal moieties seem to be more active in improving the CO_2RR catalytic performance.[15,16] For example, it has been demonstrated that bulk Pt or Cu with smaller coordi- nation numbers will enhance *CO bonding strength, and thus optimize their CO_2RR catalytic performance.[17,18] Bao *et al.* studied the CO_2RR catalytic performance on coordinately unsaturated Ni– N_x active sites anchored within porous carbon and concluded that the catalysts with unsaturated Ni–N_x sites exhibited high current density and faradaic efficiency in the CO_2RR toward CO.[19]

Covalent triazine frameworks (CTFs) are a type of covalent organic frameworks (COFs) with porous structures and high BET surface area, and can be flexibly designed in different geometric shapes, sizes and reactive groups.[20] Unlike most COFs that are incorporated with coordinately saturated transition metals (TMs),[21–25] the inborn defects in CTF frameworks allow TMs to be embedded to form coordinately unsaturated active sites, and provide a relaxed steric hindrance in their

catalytic unit for changeable adsorption modes of reactants, both of which are considered as effective strategies to improve their catalytic performance.[26–28] Nakanishi *et al.* investigated CTFs modified with coordinately unsaturated TMs for ORR (oxygen reduction reaction), HER and CO_2RR, and found that the TM-doped CTFs had higher catalytic activity than coordinately saturated TM-doped TPP (tetraphenylporphyrin) under the same conditions.[29–33] They attributed this activity improvement to the unsaturated TM on CTFs, which had more flexible adsorption modes for breaking the scaling relation in the adsorption energies of the intermediates. However, the underlying catalytic mechanism of the unsaturated TM is still controversial. Furthermore, there is a lack of design principles to guide the synthesis of the TM-CTFs. In particular, there is no effective approach to predict quantitatively the selectivity of catalysts for CO_2RR due to its complexity of the intermediates and reactions.

In this paper, we systematically explore the catalytic performance of various TM-doped CTFs for CO_2RR toward CO by using DFT methods. The stabilities, electronic structures, reaction pathways and overpotentials were calculated to predict the catalytic activity and selectivity of the TM-CTFs for CO_2 electroreduction. The calculations were supported by previous experimental results. This work thus provides a theoretical base for understanding the underlying catalytic mechanism and an effective approach for screening of TM-COFs for CO_2RR.

2 Results and discussion

2.1 Structures and stability of TM-CTFs

We have designed a series of TM-doped CTFs, including all 3d, 4d, 5d TMs except Tc, Cd, Hg and lanthanides (La–Lu) due to their toxic/radioactive property. As shown in Fig. 1A, a TM is bonded with three surrounding nitrogen atoms to form a TM–N_3 catalytic unit. The average values of bond lengths for Ni–N and Co–N in their catalyst forms were calculated to be 2.11 Å and 2.08 Å (Table S9†), which are very close to the experimental results (2.08 ± 0.05 and 2.00 ± 0.10) for Ni-CTF and Co-CTF,[26] respectively, indicating that these structures are reasonable.

We have explored the thermodynamical and electrochemical stabilities of TM-CTFs by calculating the formation energy (E_f) and dissolution potential (U_{diss}), respectively (ESI†).[34] A stable electrocatalyst should have negative formation energy (E_f < 0) and positive dissolution potential (U_{diss} > 0), making it easy to synthesize (being thermodynamically stable) and difficult to dissolve in aqueous solution (electrochemically stable).[35] As shown in Fig. 1B, the formation energy values (*x* axis) of all the TM-CTFs considered in this study are well below zero, indicating that all the TM-CTFs are thermodynamically stable, but some of them (*e.g.*, Sc-, Y-, Zr-, Hf-CTFs) are electrochemically unstable in terms of the dissolution potential (*y* axis). Thus, most of these designed catalysts are thermodynamically and electrochemically stable; the unstable TM-CTFs will be excluded in the following analysis. Actually, some TM-CTFs have been successfully synthesized for electrocatalytic applications.[36–44]

2.2 Electronic structures and CO_2RR catalytic pathways of TM-CTFs

2.2.1. CO_2 adsorption. In electrochemical reactions, the first elementary reaction usually involves the adsorption of gaseous reactants on catalyst surfaces, which is a critical step to determine catalytic mechanisms (*e.g.*, associate or dissociate adsorption modes).[45,46] Thus, we simulated CO_2RR on various

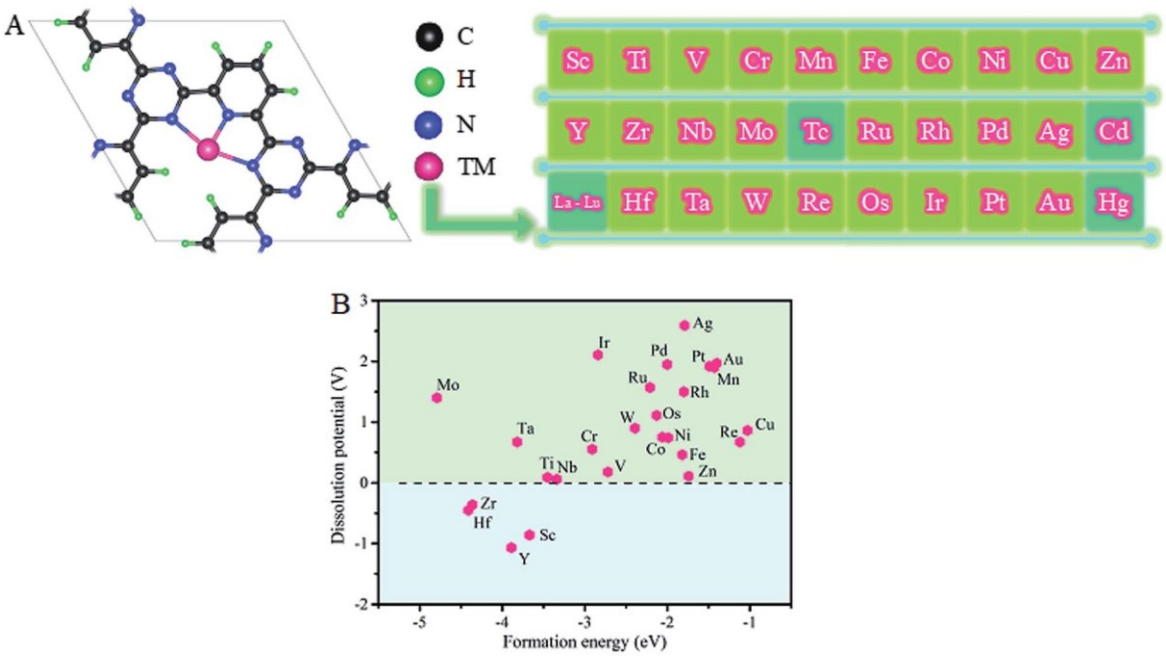

Fig. 1 (A) Molecular structure of TM-doped CTFs; the black, green, blue and pink balls represent carbon, hydrogen, nitrogen, and TM atoms; (B) calculated formation energy and dissolution potential of all TM-CTFs.

TM-CTFs, starting from CO_2 adsorption. As shown in Fig. 2A and B, there are four possible CO_2 chemisorption configurations on TM-CTFs, *i.e.*, end-on (*CO_2-1 and *CO_2-2) and side-on (*CO_2-3 and *CO_2-4) modes. Our calculations revealed that most of the TM-CTFs (TM ¼ 3d/Ti, V, Cr, Fe, Co, Ni; 4d/Nb, Mo, Ru, Rh; 5d/Ta, W, Re, Os, Ir) can directly capture CO_2 molecules with negative adsorption energy (ΔG_{*CO2} < 0 eV), indicating that the adsorption is spontaneous. CO_2 molecules can be readily adsorbed on these catalysts in mode *CO_2-3 (Fig. 2B), in which both C and O atoms in CO_2 were co-adsorbed simultaneously. In contrast, the TM-CTFs with d^9 or d^{10} electrons, including Cu, Zn, Pd, Ag, Pt, and Au, require an additional electron to promote CO_2 chemisorption. Since CO_2 chemisorption occurs after the TM acquires an electron to change its valence state, CO_2 molecules are preferentially adsorbed in mode *CO_2-3 on Cu- and Pd-CTFs, but in mode *CO_2-1 on Zn-, Ag-, Pt- and Au-CTFs. All these six catalysts also have negative adsorption energy (ΔG_{*CO2} < 0 eV) for CO_2 chemisorption except Cu-CTF with a negligible positive adsorption energy (ΔG_{*CO2} ¼ 0.08 eV). Therefore, CO_2 adsorption in the first elementary reaction is spontaneous on all TM-CTFs in mode 1 or 3.

To understand the diversities of CO_2 chemisorption modes and adsorption mechanism, we analyzed the density of state (DOS) and partial density of state (PDOS) of those TM-CTFs before and after adsorbing CO_2. As shown in Fig. 2C, two new hybridized energy levels were found near the Fermi level, namely d–p* (occ) and d–p* (unocc) formed by the interaction between 1p* anti-bonding orbitals of CO_2 and d orbit of TM-CTFs, resulting in partially occupied 1p* orbitals below the Fermi level. This interaction will help strengthen CO_2 adsorption and reduce the total energy of the overall system. Thus, the location and overlapping area of d–p* (occ) have a significant

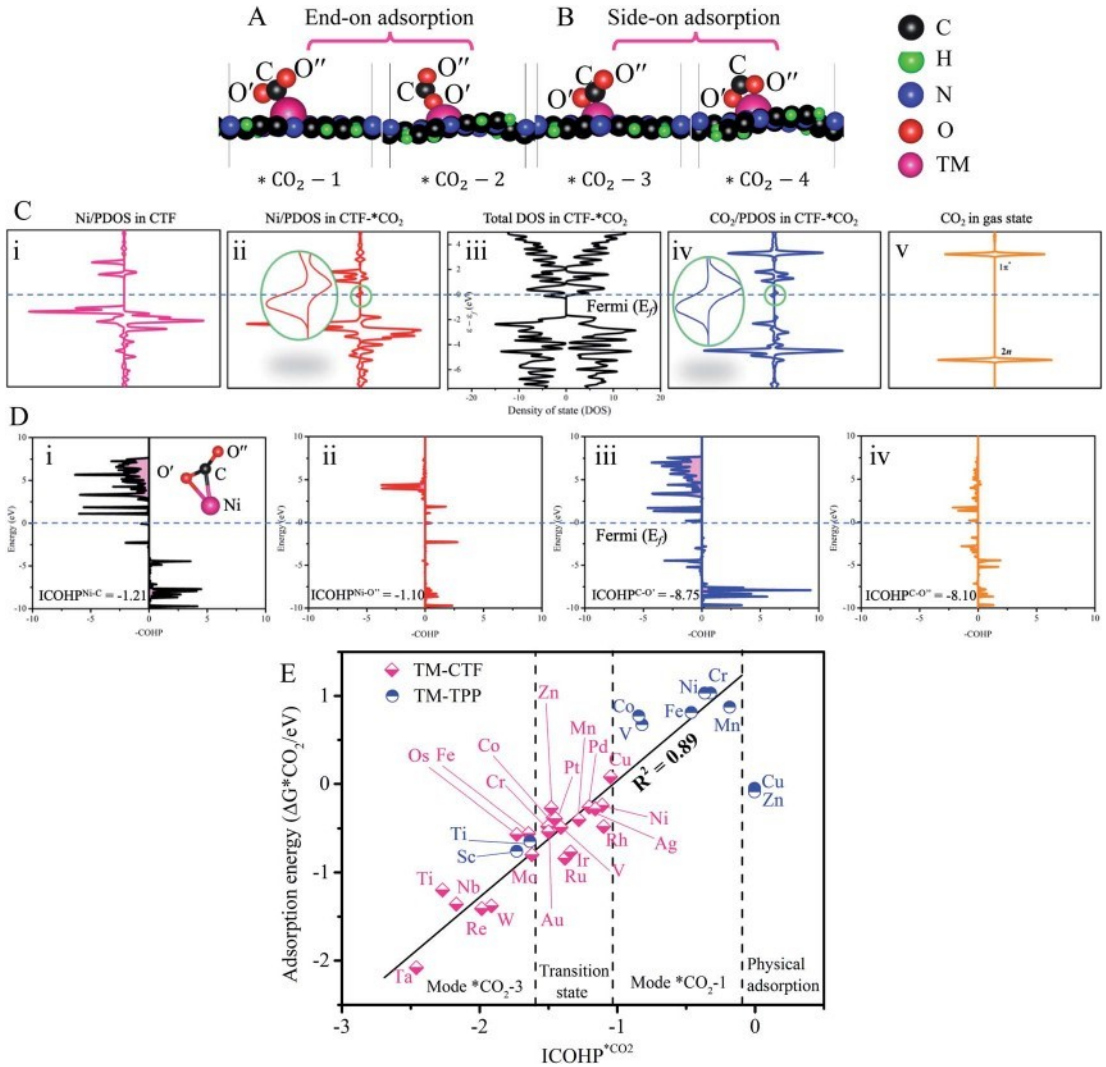

Fig. 2 Four possible *CO_2 chemisorption configurations on TM-CTFs, classified into (A) end-on and (B) side-on models. (C) The DOS and PDOS of Ni-CTFs before and after adsorbing CO_2 including (i) Ni/PDOS in Ni-CTF, (ii) Ni/PDOS in Ni-CTF-*CO_2 (adsorbing CO_2), (iii) TDOS in Ni-CTF-*CO_2, (iv) *CO_2 adsorbate/PDOS in Ni-CTF-*CO_2, (v) CO_2/PDOS in CO_2 free molecules; (D) the COHP and corresponding ICOHP values of Ni-CTF, from left to right including (i) Ni–C, (ii) Ni–O′, (iii) C–O′, and (iv) C–O″, respectively. The inset configuration of Ni-CTF-*CO_2 was simplified for clarity. (E) CO_2 adsorption energy ΔG_{*CO} as a function of ICOHP^{*CO_2} for TM-CTF and TM-TPP.[49]

effect on CO_2 adsorption capacity. Fig. S4† shows the information about the d–p* (occ) and d–p* (unocc) of 3d TM-CTFs. The d–p* (occ) of Ti-CTF has a large overlapping area and is located far from the Fermi level, which implied a strong interaction with the adsorbed CO_2. In contrast, the positive adsorption energy (ΔG_{*CO_2} ¼ 0.08 eV) of CO_2 on the Cu-CTF surface can mainly be explained by the small overlapping area and nearby location of d–p* (occ). Others have moderate overlapping area and location of d–p* (occ) leading to appropriate adsorption energy (Fig. S4†).

We further analyzed the crystal orbital Hamilton population (COHP) to gain an in-depth understanding of the d–p* interaction between the $*CO_2$ adsorbates and TM-CTFs. Fig. 2C and S6† show the COHP of typical TM-CTFs. For C–O^0 and C–O^{00} bonds (O^0 and O^{00} refer to the oxygen atoms close to and far from the metal ion, respectively, as illustrated in Fig. 2A) in $*CO_2$ adsorbates, some electrons have already occupied the antibonding orbital (–COHP < 0) below the Fermi level, in sharp contrast to free CO_2 gaseous molecules with all the electrons distributed in the bonding orbital (–COHP > 0) in Fig. S5,† indicating that these two bonds are slightly weakened. This is very important to understand the mechanism of the next hydrogenation reaction, which will be discussed later.

To quantify the d–p* interaction, the integrated-COHP (ICOHP) was calculated by integrating the electronic states up to the highest occupied energy level (Fermi level). Normally, there is a negative correlation between the ICOHP value and the strength of d–p* interaction, that is, a more negative ICOHP leads to a stronger d–p* coupling. As shown in Fig. 2D, the ICOHP values for the bonds of Ni–C and Ni–O^0 are −1.21 and −1.10, respectively, whereas Ti-CTF has the highest ICOHP values of Ti–C bond (−1.62) and Ti–O^0 bond (−2.93) (shown in Fig. S6†), indicating the strongest d–p* interaction among the 3d TM-CTFs. This could explain why Ti-CTF catalyst has the lowest CO_2 adsorption energies. To compare the difference between modes $*CO_2$-1 and $*CO_2$-3, we utilized the average ICOHP values of TM–C and TM–O bonds to represent the whole d–p* interaction (Table S6†). There is an approximately linear correlation (with R^2 of 0.89) between the ICOHP value ($ICOHP^{*CO_2}$) and the CO_2 adsorption energies (ΔG_{*CO_2}), as shown in Fig. 2E, revealing the important role played by d–p* coupling in the adsorption of CO_2 intermediate on all TM-CTFs. Interestingly, Fig. 2E can be divided into several regimes, each of which corresponds to an adsorption mode. Notably, the adsorption energy of coordinately saturated TM-TPPs[49] also follows the linear relationship with $ICOHP^{*CO_2}$ but is much higher than that of TM-CTFs. Thus, the ICOHP could be used to predict the strength and modes of CO_2 chemisorption on TM-CTFs.

2.2.2. CO_2 activation and reaction pathways. We found that there were four possible reaction pathways in CO_2RR toward CO after CO_2 adsorption, as illustrated in Fig. 3A. The first pathway (denoted as Path 1) is O^0 protonation in CO_2 activation, followed by the dissociation of *COOH to form *OH and *CO. *OH further reacts to form H_2O while *CO desorbs from TM-CTFs. This occurs on Ti, V, Cr, Nb, Ta, W, and Re-CTFs. Taking Ti-CTF as an example, the free energy change of O^0 protonation is −0.68 eV, which is much lower than that of O^{00} (0.13 eV). As a proton attacks O^0 atom, the weakened bond of C–O^0 in mode $*CO_2$-3 is broken into two independent intermediates of *OH and *CO, which are adsorbed on the same TM ion, as shown in Fig. 3A (Path 1). In Paths 2 and 3, which occur on Mn, Fe, Co, Ni, Cu, Mo, Ru, Rh, Pd, Os, and Ir-based TM-CTFs, both O^0 and O^{00} can be attacked by protons in the hydronation reaction because the reaction energy to attack O^0 atom is almost the same as attacking O^{00} atom. For example, for Ni-CTF the energy difference for attacking O^0 and O^{00} is 0.07 eV. When O^0 or O^{00} is protonated, TM–O^0 will break to form *COOH with only carbon atom bonded to TM, as shown in Fig. 3A. For the TM-CTFs with mode $*CO_2$-1, Zn-CTF, for example, has identical bond length for C–O^0 and C–O^{00} bonds, leading to the same free energy change in O protonation, as shown in Fig. 3A (Path 4). From the above analysis, CO_2RR pathways toward CO are mainly determined by the first protonation besides the configuration of CO_2 chemisorption. Since the free energy change of O^0 protonation is usually lower than that of O^{00}, O^0 atom is more likely to be attacked by protons in aqueous solutions.

To understand why O^0 is the target of proton attack in CO_2 activation, we analyzed the charge density distribution of $*CO_2$ adsorbates. Fig. S7† shows the optimized adsorption configurations and charge density distribution of CO_2 chemisorbed on TM-CTFs. It is well-known that TMs can act as an electrophile to accept electrons from adsorbates, and can also serve as a nucleophile to donate lone-pair of electrons to adsorbates. This accept–donate process results in different amounts of electrons (0.30e to 1.10e) to be transferred from the catalyst to the CO_2 adsorbates. This electron transfer can remarkably activate the double bond of O]C in CO_2, leading to a significant elongation of bond length and change of bond angle. As shown in Fig. S7,† upon adsorption on Ni-CTF, the C–O bonds in CO_2 were stretched to 1.24 Å (C–O^0) and 1.20 Å (C–O^{00}) from its gaseous state (1.16 Å), whereas the C–O bonds were elongated even more to 1.36 Å (C–O^0) and 1.21 Å (C–O^{00}) in Ti-CTF-$*CO_2$. The lower bonding strength corresponds to higher ICOHP (*e.g.*, $ICOHP^{C-O^0}$ ¼ −8.10 *vs.* $ICOHP^{C-O^{00}}$ ¼ −8.75 in Ni-CTF-$*CO_2$ as shown in Fig. 2D and S6†). Thus, ICOHP could be used to determine which O atom is the potential target in the CO_2 activation. In fact, there is an approximately linear correlation (with R^2 of 0.86) between the ICOHP of C–O^0 bond in CO_2 intermediates ($ICOHP^{C-O^0}$) and its corresponding bond length, as shown in Fig. 3B. The TMs, located on the left region ($ICOHP^{C-O^0}$ < −5), favor the formation of *COOH intermediates in CO_2 activation, whereas the dissociation and independent intermediates *CO and *OH are preferred on the TMs in the right region ($ICOHP^{C-O^0}$ > −5).

The free energy diagrams of the typical structures (Ti-, Ni-, Cu- and Zn-CTFs), that represent the four reaction pathways, are shown in Fig. 3C. The third elementary reaction, *COOH hydronation (*COOH / *CO + H_2O), is the rate-determining step (RDS) for Ti-CTF and Zn-CTF, and their reaction pathways follow Paths 1 and 4, respectively. The fourth step, *CO desorption (*CO / * + CO) in Paths 2 and 3 is the RDS for Ni-CTF and Cu-CTF, respectively. The adsorption configurations of intermediates on TM-CTFs *via* the above four catalytic

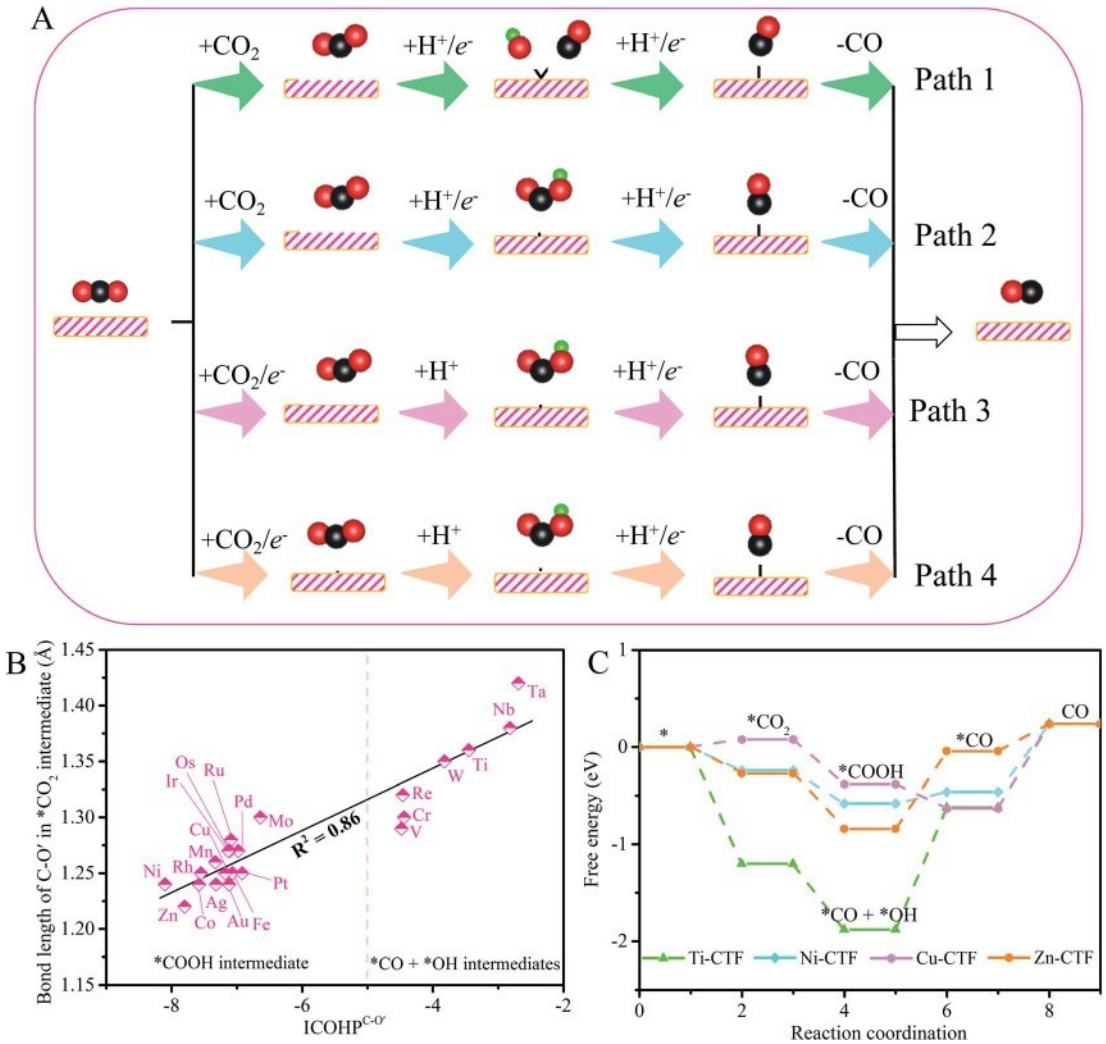

Fig. 3 (A) Four CO_2RR catalytic mechanisms to form CO (Paths 1–4). (B) The ICOHP of C–O′ in $*CO_2$ intermediates as a function of its corresponding bond length. (C) The free energy diagrams of representative catalysts: including Ti-CTF, Ni-CTF, Cu-CTF, and Zn-CTF.

mechanisms are shown in Fig. S8–S11.† Note that Mn-CTF is the only case with RDS in the third elementary step of Path 2.

2.3 Catalytic activity and intrinsic descriptors

Establishing the relationship between catalytic performance and descriptors would provide a theoretical guideline and tool for screening the best catalysts from a large number of catalyst candidates. While the catalytic performance is usually measured by overpotential (h),[47,48] a predictive descriptor is more decisive to catalyst screening. We first explore the relationship between the overpotential of the CO_2RR (h^{CO}) and the adsorption energy of $DG_{*CO} - DG_{*COOH}$, as both *COOH and *CO adsorption plays an important role in determining the reaction pathways. As shown in Fig. 4A, volcano-shaped relationships are established for coordinately unsaturated TM-CTFs and coordinately saturated TM-TPPs[49] with Ni-CTF (h^{CO} ¼ 0.34 V) and Co-TPP (h^{CO} ¼ 0.78 V) located at the top of the volcano, respectively. Overall, TM-CTFs with coordinately unsaturated TMs are much better than the TM-TPPs with coordinately saturated TM sites. Ni-CTF stands out as the best catalyst for the CO_2RR among these catalysts. This prediction is supported by the previous experimental results that Co-CTF, Ni-CTF, and Cu-CTF have higher Faraday efficiency (FE^{CO}) and current density (*j*) under the same conditions than the corresponding Co-TPP, Ni-TPP and Cu-TPP.[26] Furthermore, most of the TM-CTFs have better CO_2RR catalytic activity than noble metals such as Ag[50] and Au,[51] which are regarded as the state-of-the-art catalysts for CO_2RR. Thus, TM-CTFs are a class of catalyst candidates with highly catalytic activity and expected to replace the noble metal catalysts.

Although a volcanic relationship has been established by using the adsorption energy as a descriptor, it is of more interest to identify an intrinsic descriptor that has a predictive power without further DFT calculations to guide the screening of the best catalysts from numerous material candidates. Recently, the d-band center,[52] crystal field stabilization energy (CFSE),[45] e_g occupancy,[53] t_{2g} occupancy[54] and p-band center[55,56] have been employed as descriptors to describe the catalytic

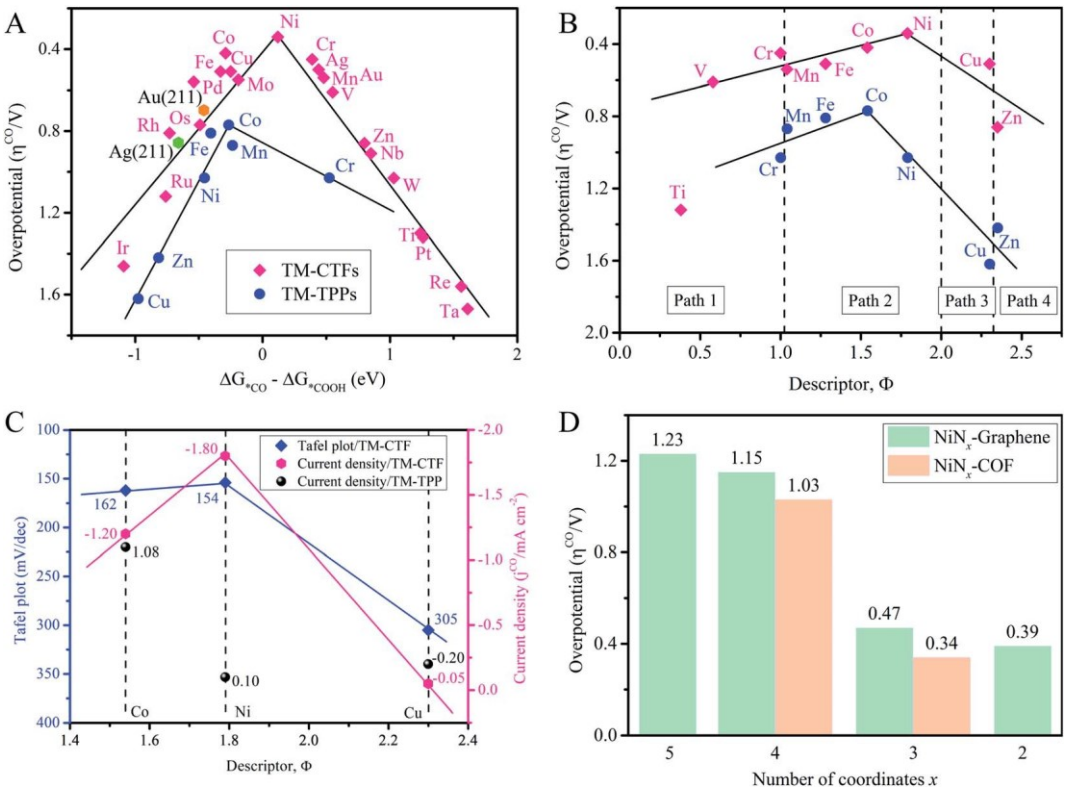

Fig. 4 (A) Volcano-shaped relationships between the overpotential (h^{CO}) and the adsorption energy of $\Delta G_{*CO} - \Delta G_{*COOH}$ for TM-CTFs, TM-TPPs, Au and Ag. (B) Volcano-shaped relationship between overpotential (h^{CO}) and descriptor for 3d TM-CTFs and 3d TM-TPPs. (C) The measured Tafel plot (mV dec^{-1}) and current density (j^{CO}/mA cm^{-2}) as a function of the descriptor.[26] (D) The overpotential (h^{CO}) of NiN_x based catalysts with different coordination numbers (x ¼ 2 to 5), together with Ni-TPP and Ni-CTF.

activity of ORR, OER, and HER on TM or TM-based catalysts. However, little work is done on coordinately unsaturated TM-CTFs for more complex CO_2RR. To establish a volcanic relationship with the overpotential (h^{CO}) for TM-CTFs, we have discovered a simple but inherent descriptor (F) de□ned by:

$$F = \frac{N}{r_{TM} \times n}$$

where N, r_{TM}, and n are the number of d electrons, atomic radius, and periodic number of TMs (detailed in the ESI†). There is a positive correlation between the descriptor and the adsorption energy of intermediates or the bond strength of TM-intermediates, as shown in Fig. S12A.† Therefore, this descriptor, relating to the adsorption or bond strength of intermediates, represents the intrinsic characteristic of TM-CTFs, which has a certain physical meaning. Fig. S12B† is the volcanic relationship between the descriptor and overpotential (h^{CO}) for all TM-CTFs, and Ni-CTF (h^{CO} ¼ 0.34 V) locates on the top of the volcano followed by Co-CTF (h^{CO} ¼ 0.42 V) and Cu-CTF (h^{CO} ¼ 0.51 V), which would show excellent catalytic activity in the electroreduction of CO_2 to CO because their overpotentials are lower than those of noble metal (Ag and Au) catalysts. Accordingly, the catalysts with the range of F ¼ 0.08 to 1.30 could have high CO_2RR catalytic activity (h^{CO} < 0.55 V), which perform better than noble metals, Au (h^{CO} ¼ 0.70 V) and Ag (h^{CO} ¼ 0.86 V). In addition, the new descriptor also works well for coordinately saturated TM-TPPs (Fig. S12†).

In addition to the prediction of the best catalysts, the catalytic mechanism can also be intuitively distinguished by using this descriptor for both coordinately saturated and unsaturated COFs. As shown in Fig. 4B, four regimes are clearly differentiated, which correspond to four reaction mechanisms: (a) Regime 1 with F < 1.02, in which CO_2RR toward CO proceeds *via* Path 1, on Ti, V, Cr-CTF catalysts; (b) Regime 2 with 1.02 < F < 2.00, where CO_2RR prefers Path 2 on Mn, Fe, Co, Ni-CTFs; (c) Regime 3 with 2.00 < F < 2.32, where Path 3 dominates CO_2RR on Cu-CTF; (d) Regime 4 with F > 2.32, where CO_2RR follows Path 4 on Zn-CTFs. Moreover, the CO_2RR catalytic mechanism on 4d or 5d TM-CTFs can also be predicted, as shown in Fig. S13.† Therefore, the descriptor (F) provides an effective tool for quickly predicting the CO_2RR catalytic activity and mechanisms of TM-CTFs.

The above predictions are consistent with the previous experimental results (Table S10†). We have extracted current density (j) and the lowest Tafel plots from the literature.[26] As shown in Fig. 4C, similar volcano-shaped relationships between the experimental results and the descriptor are established, in which the Ni-CTF exhibits the best catalytic performance, as predicted in this study. Thus, this novel descriptor can serve as

a reliable design principle to guide the synthesis of high-performance catalysts.

We also explore the effect of the number of coordinates of TMs in COFs on CO_2RR. As shown in Fig. S14,† four NiN_x based catalysts with different coordination numbers (x ¼ 2 to 5) anchored on graphene substrates are designed to calculate their CO_2RR catalytic behavior. The catalysts with high coordination number (*e.g.* NiN_5 and NiN_4) have poor activity for CO_2 chemisorption and CO_2 activation, resulting in a large overpotential (η^{CO} ¼ 1.29 eV/NiN_5 or 1.15 eV/NiN_4) and poor CO_2RR catalytic performance. Those catalysts with a coordinately unsaturated TM in their units, namely NiN_3 and NiN_2, provide flexible modes in decreasing the adsorption energy of CO_2 and the intermediates. Thus, coordinately unsaturated catalysts exhibit higher CO_2RR catalytic activity than the catalysts with coordinately saturated TM units, as shown in Fig. 4d.

2.4 Competing reactions and selectivity predictions

Formic (HCOOH) acid or formate is a possible product that competes with CO in the CO_2RR. Thus, we simulated the electrocatalytic CO_2RR to HCOOH under the same conditions. The CO_2RR towards HCOOH on TM-CTFs follows the following pathway: CO_2 / *CO_2 / *OCHO / *HCOOH / $HCOOH_{(l)}$. Notably, the process of producing HCOOH from *COOH can be excluded since according to the transition state (TS) calculation, there is a large energy barrier for the protonation of the inner C atom than that of the external O atom at the second hydronation reaction (Fig. S17†).

Thermodynamically, a catalyst with high selectivity should have lower overpotential for CO than its competitors. Therefore, we plotted the overpotential of CO (η^{CO}) *versus* that of HCOOH (η^{HCOOH}) to determine whether CO or HCOOH is the dominant product in the CO_2RR. As shown in Fig. S18A,† most of the TM-CTFs are located at the CO-dominated region ($\eta^{CO} < \eta^{HCOOH}$) except for Ru-, Rh-, Ta-, Ir-, and Pt-CTFs that promote HCOOH formation. Fig. S15† shows the free energy diagrams of these five catalysts for HCOOH. In fact, experiments have confirmed that the Rh-, Ru-, Ir-, Pt-based catalysts favor the production of HCOOH in the electrocatalytic CO_2RR.[57–60] In particular, Rh-CTF (0.57 V), Ru-CTF (0.54 V), Ir-CTF (0.43 V), and Pt-CTF (0.49 V) catalysts have activities comparable to Pt-based noble catalysts (0.17 V) and $CuSn_3$ catalysts (0.39 V) in the electroreduction of CO_2 to HCOOH. The volcano-shaped relationships can also be established by the adsorption energy difference of $\Delta G_{*HCOOH} - \Delta G_{*OCHO}$ or descriptor (F) *versus* the overpotential of HCOOH (η^{HCOOH}), as shown in Fig. S16.†

In addition, H_2 also competes with CO and HCOOH in the CO_2RR since the thermodynamic potential of the HER is very close to that of CO_2RR.[61] Similarly, the overpotential (η^{CO} *vs.* η^{H_2} or η^{HCOOH} *vs.* η^{H_2}) was also utilized to predict the preference of CO_2RR and HER on TM-CTFs. The overpotential of HER (η^{H_2}) was calculated and is listed in Table S7,† together with that of CO_2RR (η^{CO}, η^{HCOOH}). As shown in Fig. S18,† Mn-, Fe-, Co-, Ni-, Ag- and Au-CTFs locate at the CO-dominated region ($\eta^{CO} < \eta^{H_2}$) and would have a strong ability to suppress HER. On the other hand, Ir- and Pt-CTFs have lower overpotential for HCOOH than for H_2 ($\eta^{HCOOH} < \eta^{H_2}$), and may preferentially catalyze CO_2RR toward HCOOH. Thus, eight TM-CTFs are promising candidates with high activity and selectivity for CO_2RR to produce CO or HCOOH.

It is of importance to quantitatively predict the selectivity of the catalysts such that the efficiency of the final products could be determined under different conditions. So far, there is no quantitative measure from computational approaches to determine the selectivity of the catalysts. Here, we introduce a simple parameter, the ratio of overpotentials of H_2 (η^{H_2}) to CO (η^{CO}) as an indicator of selectivity since it represents the relative compatibility between two competing chemical products (CO and H_2) at the same active sites under the same conditions. Fig. 5A shows the ratio (η^{H_2}/η^{CO}) as a function of the descriptor (F). We found that the descriptor also established a volcanic relationship with the selectivity with a flat summit in the regime of $1 < F < 2$, in which TM-CTFs and TM-TPPs are expected to exhibit high selectivity for CO_2RR to CO. Our prediction fits well with the previous experimental data that the ratio of onset potential measured in experiments *versus* the descriptor also exhibits a similar volcanic relationship, as shown in Fig. 5B.

The above predictions are also consistent with the previous experiments on Faraday efficiency (FE). It is well-known that the Faraday efficiency of CO is an important indicator that represents the overall conversion efficiency or selectivity of the catalytic systems in competition with HER. We have cited the Faraday efficiency of various M–N–C SACs and TM-CTFs from the literature and made a plot of the reported FE *versus* the descriptor (Fig. 5C). In spite of data scattering due to different measuring conditions, the results show a volcano-shaped plot, which is consistent with the predictions for the volcano in Fig. 5A. Therefore, the ratio of overpotentials of H_2 (η^{H_2}) to CO (η^{CO}) can be used as an effective index to predict the selectivity of the catalysts under different conditions.

The effect of the TM coordinates on the catalytic efficiency is also verified experimentally. As shown in Fig. 5D, the Faraday efficiency of the catalysts increases with reducing the coordination number, *i.e.*, the coordinately unsaturated catalysts have higher Faraday efficiency than the coordinately saturated catalysts. These experimental results are consistent with our predictions shown in Fig. 4D. This demonstrates the predictive power of the descriptor for not only catalytic activity but also selectivity, guiding the rational design of highly active and selective TM-CTFs for CO_2 conversion.

It should be noted here that the current study focuses on CTFs with single TM. It is possible to further enhance the catalytic activity by introducing dual or tri TM in CTFs to form bimetallic or trimetallic catalysts (Fig. S19†). Thus, we further explored the CO_2RR catalytic activity on those TM-CTFs with single, double, and triple TMs. As shown in Fig. S20,† the overpotential (η^{CO}) change ranged from −0.02 V to 0.04 V for Fe, Co, and Ni active sites. Thus, the influence of the second (Ni_2-CTF, Ni,Fe-CTF, Ni,Co-CTF) or third metal (Ni_3-CTF) is almost negligible. We also considered the effect of atomic size and selected doping elements with relatively large atomic radius, including Mo (r ¼ 1.90 Å) and Os (r ¼ 1.85 Å) to replace Ni (r ¼ 1.63 Å) in the other two active sites. The overpotential of the

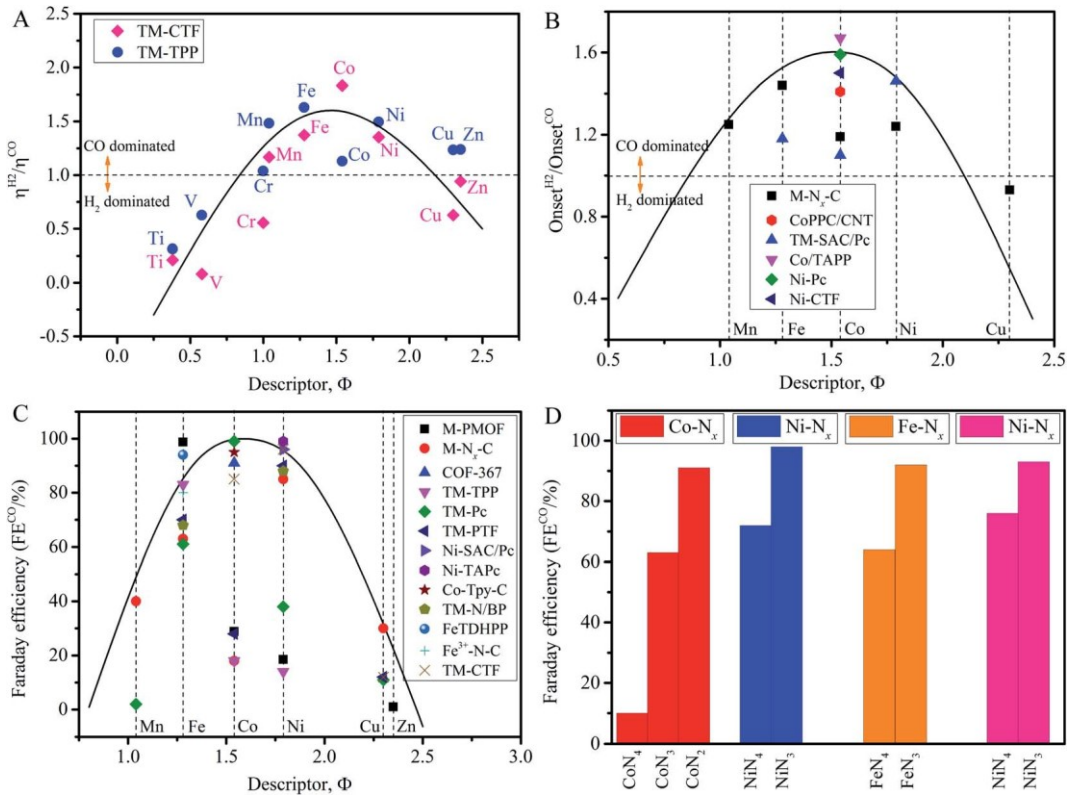

Fig. 5 (A) The ratio between the calculated overpotential of H_2 (h^{H_2}) and CO (h^{CO}) as a function of the descriptor, predicted by the DFT calculations; (B) the ratio between the experimental onset potential of H_2 (h^{H_2}) and CO (h^{CO}) as a function of the descriptor, measured in the experiments;[49,62–65] (C) the experimental results of Faraday efficiency (FE^{CO}) as a function of the descriptor;[13,49,62–69] (D) Faraday efficiency (FE^{CO}) of the FeN_x, CoN_x and NiN_x based catalysts with different coordination numbers.[70–73]

three active sites in Ni, Mo, Os-CTF trimetallic catalysts increases by approximately 0.10 V compared with Ni-CTF. Therefore, the catalytic activity will not be affected signi□cantly by introducing one or more TMs with large atomic radius. Although the activity is not improved signi□cantly with a heterometal, the bi- or tri-metal sites could be designed to achieve cascade reactions in which different sites are specialized to catalyze different reactions, like a two-pot tandem reaction of CO_2RR on alloys.[74]

3 Conclusion

The CO_2RR catalytic behaviors on TM-CTFs have been systematically investigated by means of the DFT method to understand the catalytic mechanism and predict the catalytic activity and selectivity. Volcano-shaped relationships have been established by using the intrinsic characteristics as effective descriptors, from which the best activity and selectivity of the catalyst could be directly predicted. The corresponding catalytic mechanism of catalysts could also be easily distinguished from the volcanic map. Among the catalysts, Ni-CTF has the highest catalytic activity (h^{CO} ¼ 0.34 V) in the electroreduction of CO_2 to CO, and most of the TM-CTFs with coordinately unsaturated TM active sites exhibit better CO_2RR catalytic activity than TM-TPPs with coordinately saturated TM sites. Eight catalysts, namely Mn-CTF (h^{CO} ¼ 0.54 V), Fe-CTF (h^{CO} ¼ 0.51 V), Co-CTF (h^{CO} ¼ 0.42 V), Ni-CTF (h^{CO} ¼ 0.34 V), Ag-CTF (h^{CO} ¼ 0.50 V), Au-CTF (h^{CO} ¼ 0.54 V), Ir-CTF (h^{HCOOH} ¼ 0.43 V) and Pt-CTF (h^{HCOOH} ¼ 0.49 V), are expected to be promising candidates for CO_2RR, which have lower overpotential to inhibit the undesirable competitive reaction, HER. The predictions are supported by previous experimental results from the literature. This work provides a principle for guiding the rational design and screening of highly active and selective catalysts for CO_2RR.

4 Computational methods

The Vienna *Ab initio* Simulation Package (VASP) code based on the density functional theory (DFT) was utilized to explore the catalytic behavior of the CO_2RR on TM-CTFs.[75,76] The gradient corrected approximation of Perdew–Burke–Ernzerhof (GGA-PBE) functional was utilized to calculate the exchange–correlation energy, and the project-augmented wave generalized gradient approximation pseudopotentials (PAW-GGA) were adopted to describe the electron–ion interaction.[77,78] The Hubbard *U* (DFT+*U*) corrections were considered in the calculations and the values of the correction are listed in Table S1.†[45] Wave functions were expanded using a plane-wave basis set with a kinetic energy cutoff of 550 eV with a gamma *K*-point grid of 3 x 3 x 1 for the Brillouin zone sampling for structural

optimization or 5 x 5 x 1 for calculation of the density of states (DOS). The self-consistent field (SCF) was fully relaxed until the residual force convergence threshold of 0.01 eV Å^{-1}. A vacuum spacing of at least 20 Å in the perpendicular *z*-direction was employed to avert the artificial interactions between the periodically repeated images. Spin-polarization was considered in all calculations. The above parameters have been optimized until the energy change is negligible. The CO_2RR catalytic behavior on commercial noble electrocatalysts such as Ag (2 1 1) and Au (2 1 1) was also simulated and the results are listed in Table S8.† A p(4 x 4) unit cell was chosen for both catalysts. Four layers were built in their slab configuration. The crystal orbital Hamilton population (COHP) analysis was carried out using the LOBSTER program (Local Orbital Basis Suite Towards Electronic-Structure Reconstruction).[79,80] More details about computational methods for thermodynamic-related values are described in the ESI.†

Author contributions

Z. X. and L. G. conceived and designed the research. L. G., J. L. and T. Z. performed modelling and simulation, L. G. and Z. X. wrote the manuscript. All authors discussed the results and commented on the manuscript.

Conflicts of interest

The authors declare no competing interests.

Acknowledgements

L. G., T. Z., X. H., and J. Z. thank the National Key Research and Development Program of China (2017YFA0206500), National Natural Science Foundation of China (51732002, 52073020, 52002324), Distinguished Scientist Program at BUCT (buctylkxj02), Natural Science Basic Research Program of Shaanxi (2020JQ-163) and China Scholarships Council (No. 201806880044). Z. X., J. L. and X. W. thank U.S. National Science Foundation (1561886 and 1662288) for the support of this research.

References

1 H. A. Hansen, J. B. Varley, A. A. Peterson and J. K. Nørskov, Understanding Trends in the Electrocatalytic Activity of Metals and Enzymes for CO_2 Reduction to CO, *J. Phys. Chem. Lett.*, 2013, 4, 388–392.

2 K. P. Kuhl, E. R. Cave, D. N. Abram and T. F. Jaramillo, New insights into the electrochemical reduction of carbon dioxide on metallic copper surfaces, *Energy Environ. Sci.*, 2012, 5, 7050–7059.

3 M. Ma, K. Djanashvili and W. A. Smith, Controllable Hydrocarbon Formation from the Electrochemical Reduction of CO_2 over Cu Nanowire Arrays, *Angew. Chem.*, 2016, 128, 6792–6796.

4 C. Hu, L. Gong, Y. Xiao, Y. Yuan, N. M. Bedford, Z. Xia, L. Ma, T. Wu, Y. Lin, J. W. Connell, R. Shahbazian-Yassar, J. Lu, K. Amine and L. Dai, High Performance, Long Life, Rechargeable Li–CO_2 Batteries based on a 3D Holey Graphene Cathode Implanted with Single Iron Atoms, *Adv. Mater.*, 2020, 32, 1907436.

5 L. L. Gong, X. F. Feng and F. Luo, Novel azo-Metal–Organic Framework Showing a 10-Connected bct Net, Breathing Behavior, and Unique Photoswitching Behavior toward CO_2, *Inorg. Chem.*, 2015, 54, 11587–11589.

6 J. Bonin, A. Maurin and M. Robert, Molecular catalysis of the electrochemical and photochemical reduction of CO_2 with Fe and Co metal based complexes. Recent advances, *Coord. Chem. Rev.*, 2017, 334, 184–198.

7 J. Choi, P. Wagner, R. Jalili, J. Kim, D. R. MacFarlane, G. G. Wallace and D. L. Officer, A porphyrin/graphene framework: a highly efficient and robust electrocatalyst for carbon dioxide reduction, *Adv. Energy Mater.*, 2018, 8, 1801280.

8 A. Vasileff, Y. Zheng and S. Z. Qiao, Carbon Solving Carbon's Problems: Recent Progress of Nanostructured Carbon-Based Catalysts for the Electrochemical Reduction of CO_2, *Adv. Energy Mater.*, 2017, 7, 1700759.

9 S. Lin, C. S. Diercks, Y.-B. Zhang, N. Kornienko, E. M. Nichols, Y. Zhao, A. R. Paris, D. Kim, P. Yang, O. M. Yaghi and C. J. Chang, Covalent organic frameworks comprising cobalt porphyrins for catalytic CO_2 reduction in water, *Science*, 2015, 349, 1208–1213.

10 K. Jiang and H. Wang, Electrocatalysis over graphene-defect-coordinated transition-metal single-atom catalysts, *Chem*, 2018, 4, 194–195.

11 T. N. Huan, N. Ranjbar, G. Rousse, M. Sougrati, A. Zitolo, V. Mougel, F. Jaouen and M. Fontecave, Electrochemical Reduction of CO_2 Catalyzed by Fe-NC Materials: A Structure–Selectivity Study, *ACS Catal.*, 2017, 7, 1520–1525.

12 X.-M. Hu, M. H. Rønne, S. U. Pedersen, T. Skrydstrup and K. Daasbjerg, Enhanced Catalytic Activity of Cobalt Porphyrin in CO_2 Electroreduction upon Immobilization on Carbon Materials, *Angew. Chem., Int. Ed.*, 2017, 56, 6468–6472.

13 S. Liu, H. B. Yang, S.-F. Hung, J. Ding, W. Cai, L. Liu, J. Gao, X. Li, X. Ren, Z. Kuang, Y. Huang, T. Zhang and B. Liu, Elucidating the Electrocatalytic CO_2 Reduction Reaction over a Model Single-Atom Nickel Catalyst, *Angew. Chem., Int. Ed.*, 2020, 59, 798–803.

14 Y. Wang, P. Han, X. Lv, L. Zhang and G. Zheng, Defect and Interface Engineering for Aqueous Electrocatalytic CO_2 Reduction, *Joule*, 2018, 2, 2551–2582.

15 W. Zheng, J. Yang, H. Chen, Y. Hou, Q. Wang, M. Gu, F. He, Y. Xia, Z. Xia, Z. Li, B. Yang, L. Lei, C. Yuan, Q. He, M. Qiu and X. Feng, Atomically Defined Undercoordinated Active Sites for Highly Efficient CO_2 Electroreduction, *Adv. Funct. Mater.*, 2020, 30, 1907658.

16 X. Rong, H.-J. Wang, X.-L. Lu, R. Si and T.-B. Lu, Controlled Synthesis of a Vacancy-Defect Single-Atom Catalyst for Boosting CO_2 Electroreduction, *Angew. Chem., Int. Ed.*, 2020, 59, 1961–1965.

17 Z. Zhao, Z. Chen, X. Zhang and G. Lu, Generalized Surface Coordination Number as an Activity Descriptor for CO_2

Reduction on Cu Surfaces, *J. Phys. Chem. C*, 2016, 120, 28125–28130.

18 H. Li, Y. Li, M. T. M. Koper and F. Calle-Vallejo, Bond-making and breaking between carbon, nitrogen, and oxygen in electrocatalysis, *J. Am. Chem. Soc.*, 2014, 136, 15694–15701.

19 C. Yan, H. Li, Y. Ye, H. Wu, F. Cai, R. Si, J. Xiao, S. Miao, S. Xie, F. Yang, Y. Li, G. Wang and X. Bao, Coordinatively unsaturated nickel–nitrogen sites towards selective and high-rate CO_2 electroreduction, *Energy Environ. Sci.*, 2018, 11, 1204–1210.

20 K. Iwase, S. Nakanishi, M. Miyayama and K. Kamiya, Rational Molecular Design of Electrocatalysts Based on Single-Atom Modified Covalent Organic Frameworks for Efficient Oxygen Reduction Reaction, *ACS Appl. Energy Mater.*, 2020, 3, 1644–1652.

21 Y.-R. Wang, Q. Huang, C.-T. He, Y. Chen, J. Liu, F.-C. Shen and Y.-Q. Lan, Oriented electron transmission in polyoxometalate-metalloporphyrin organic framework for highly selective electroreduction of CO_2, *Nat. Commun.*, 2018, 9, 4466.

22 C. S. Diercks, S. Lin, N. Kornienko, E. A. Kapustin, E. M. Nichols, C. Zhu, Y. Zhao, C. J. Chang and O. M. Yaghi, Reticular electronic tuning of porphyrin active sites in covalent organic frameworks for electrocatalytic carbon dioxide reduction, *J. Am. Chem. Soc.*, 2018, 140, 1116–1122.

23 Y. Liu, X. Yan, T. Li, W.-D. Zhang, Q.-T. Fu, H.-S. Lu, X. Wang and Z.-G. Gu, Three-dimensional porphyrin-based covalent organic frameworks with tetrahedral building blocks for single-site catalysis, *New J. Chem.*, 2019, 43, 16907–16914.

24 K. Rybicka-Jasińska, W. Shan, K. Zawada, K. M. Kadish and D. Gryko, Porphyrins as Photoredox Catalysts: Experimental and Theoretical Studies, *J. Am. Chem. Soc.*, 2016, 138, 15451–15458.

25 N. Zion, D. A. Cullen, P. Zelenay and L. Elbaz, Heat-Treated Aerogel as a Catalyst for the Oxygen Reduction Reaction, *Angew. Chem., Int. Ed.*, 2020, 59, 2483–2489.

26 P. Su, K. Iwase, T. Harada, K. Kamiya and S. Nakanishi, Covalent triazine framework modified with coordinatively-unsaturated Co or Ni atoms for CO_2 electrochemical reduction, *Chem. Sci.*, 2018, 9, 3941–3947.

27 P. Puthiaraj, Y.-R. Lee, S. Zhang and W.-S. Ahn, Triazine-based covalent organic polymers: design, synthesis and applications in heterogeneous catalysis, *J. Mater. Chem. A*, 2016, 4, 16288–16311.

28 K. Wang, L.-M. Yang, X. Wang, L. Guo, G. Cheng, C. Zhang, S. Jin, B. Tan and A. Cooper, Covalent triazine frameworks via a low-temperature polycondensation approach, *Angew. Chem., Int. Ed.*, 2017, 56, 14149–14153.

29 T. Yoshioka, K. Iwase, S. Nakanishi, K. Hashimoto and K. Kamiya, Electrocatalytic reduction of nitrate to nitrous oxide by a copper-modified covalent triazine framework, *J. Phys. Chem. C*, 2016, 120, 15729–15734.

30 K. Iwase, T. Yoshioka, S. Nakanishi, K. Hashimoto and K. Kamiya, Copper-Modified Covalent Triazine Frameworks as Non-Noble-Metal Electrocatalysts for Oxygen Reduction, *Angew. Chem., Int. Ed.*, 2015, 54, 11068–11072.

31 R. Kamai, K. Kamiya, K. Hashimoto and S. Nakanishi, Oxygen-Tolerant Electrodes with Platinum-Loaded Covalent Triazine Frameworks for the Hydrogen Oxidation Reaction, *Angew. Chem., Int. Ed.*, 2016, 55, 13378–13382.

32 K. Kamiya, R. Kamai, K. Hashimoto and S. Nakanishi, Platinum-modified covalent triazine frameworks hybridized with carbon nanoparticles as methanol-tolerant oxygen reduction electrocatalysts, *Nat. Commun.*, 2014, 5, 5040.

33 K. Iwase, K. Kamiya, M. Miyayama, K. Hashimoto and S. Nakanishi, Sulfur-Linked Covalent Triazine Frameworks Doped with Coordinatively Unsaturated Cu(I) as Electrocatalysts for Oxygen Reduction, *ChemElectroChem*, 2018, 5, 805–810.

34 X. Guo, J. Gu, S. Lin, S. Zhang, Z. Chen and S. Huang, Tackling the Activity and Selectivity Challenges of Electrocatalysts toward the Nitrogen Reduction Reaction via Atomically Dispersed Biatom Catalysts, *J. Am. Chem. Soc.*, 2020, 142, 5709–5721.

35 X. Guo, S. Lin, J. Gu, S. Zhang, Z. Chen and S. Huang, Simultaneously Achieving High Activity and Selectivity toward Two-Electron O_2 Electroreduction: The Power of Single-Atom Catalysts, *ACS Catal.*, 2019, 9, 11042–11054.

36 S. Yamaguchi, K. Kamiya, K. Hashimoto and S. Nakanishi, Ru atom-modified covalent triazine framework as a robust electrocatalyst for selective alcohol oxidation in aqueous electrolytes, *Chem. Commun.*, 2017, 53, 10437–10440.

37 R. Palkovits, M. Antonietti, P. Kuhn, A. Thomas and F. Schüth, Solid catalysts for the selective low-temperature oxidation of methane to methanol, *Angew. Chem., Int. Ed.*, 2009, 48, 6909–6912.

38 R. Kamai, S. Nakanishi, K. Hashimoto and K. Kamiya, Selective electrochemical reduction of nitrogen oxides by covalent triazine frameworks modified with single Pt atoms, *J. Electroanal. Chem.*, 2017, 800, 54–59.

39 A. V. Bavykina, A. I. Olivos-Suarez, D. Osadchii, R. Valecha, R. Franz, M. Makkee, F. Kapteijn and J. Gascon, Facile method for the preparation of covalent triazine framework coated monoliths as catalyst support: applications in C1 catalysis, *ACS Appl. Mater. Interfaces*, 2017, 9, 26060–26065.

40 K. Kamiya, T. Tatebe, S. Yamamura, K. Iwase, T. Harada and S. Nakanishi, Selective reduction of nitrate by a local cell catalyst composed of metal-doped covalent triazine frameworks, *ACS Catal.*, 2018, 8, 2693–2698.

41 K. Park, G. H. Gunasekar, N. Prakash, K.-D. Jung and S. Yoon, A highly efficient heterogenized iridium complex for the catalytic hydrogenation of carbon dioxide to formate, *ChemSusChem*, 2015, 8, 3410–3413.

42 J. Li, P. Liu, Y. Tang, H. Huang, H. Cui, D. Mei and C. Zhong, Single-Atom Pt–N_3 Sites on the Stable Covalent Triazine Framework Nanosheets for Photocatalytic N_2 Fixation, *ACS Catal.*, 2020, 10, 2431–2442.

43 C. Lu, J. Yang, S. Wei, S. Bi, Y. Xia, M. Chen, Y. Hou, M. Qiu, C. Yuan, Y. Su, F. Zhang, H. Liang and X. Zhuang, Atomic Ni Anchored Covalent Triazine Framework as High Efficient

Electrocatalyst for Carbon Dioxide Conversion, *Adv. Funct. Mater.*, 2019, 29, 1806884.

44 O. Buyukcakir, S. H. Je, S. N. Talapaneni, D. Kim and A. Coskun, Charged Covalent Triazine Frameworks for CO_2 Capture and Conversion, *ACS Appl. Mater. Interfaces*, 2017, 9, 7209–7216.

45 C.-Y. Lin, L. Zhang, Z. Zhao and Z. Xia, Design principles for covalent organic frameworks as efficient electrocatalysts in clean energy conversion and green oxidizer production, *Adv. Mater.*, 2017, 29, 1606635.

46 Z. Duan and G. Wang, Comparison of reaction energetics for oxygen reduction reactions on Pt (100), Pt (111), Pt/Ni (100), and Pt/Ni (111) surfaces: a first-principles study, *J. Phys. Chem. C*, 2013, 117, 6284–6292.

47 L. Zhang, J. Niu, M. Li and Z. Xia, Catalytic mechanisms of sulfur-doped graphene as efficient oxygen reduction reaction catalysts for fuel cells, *J. Phys. Chem. C*, 2014, 118, 3545–3553.

48 L. Zhang, C.-Y. Lin, D. Zhang, L. Gong, Y. Zhu, Z. Zhao, Q. Xu, H. Li and Z. Xia, Guiding Principles for Designing Highly Efficient Metal-Free Carbon Catalysts, *Adv. Mater.*, 2018, 31, 1805252.

49 L. Gong, D. Zhang, C.-Y. Lin, Y. Zhu, Y. Shen, J. Zhang, X. Han, L. Zhang and Z. Xia, Catalytic Mechanisms and Design Principles for Single-Atom Catalysts in Highly Efficient CO_2 Conversion, *Adv. Energy Mater.*, 2019, 9, 1902625.

50 M. R. Singh, J. D. Goodpaster, A. Z. Weber, M. Head-Gordon and A. T. Bell, Mechanistic insights into electrochemical reduction of CO_2 over Ag using density functional theory and transport models, *Proc. Natl. Acad. Sci. U. S. A.*, 2017, 114, E8812.

51 W. Zhu, R. Michalsky, Ö. Metin, H. Lv, S. Guo, C. J. Wright, X. Sun, A. A. Peterson and S. Sun, Monodisperse Au Nanoparticles for Selective Electrocatalytic Reduction of CO_2 to CO, *J. Am. Chem. Soc.*, 2013, 135, 16833–16836.

52 B. Hammer and J. K. Norskov, Theoretical surface science and catalysis—calculations and concepts, *Adv. Catal.*, 2000, 45, 71–129.

53 J. Suntivich, H. A. Gasteiger, N. Yabuuchi, H. Nakanishi, J. B. Goodenough and Y. Shao-Horn, Design principles for oxygen-reduction activity on perovskite oxide catalysts for fuel cells and metal–air batteries, *Nat. Chem.*, 2011, 3, 546–550.

54 K. Toyoda, R. Hinogami, N. Miyata and M. Aizawa, Calculated descriptors of catalytic activity for water electrolysis anode: application to delafossite oxides, *J. Phys. Chem. C*, 2015, 119, 6495–6501.

55 A. Grimaud, K. J. May, C. E. Carlton, Y.-L. Lee, M. Risch, W. T. Hong, J. Zhou and Y. Shao-Horn, Double perovskites as a family of highly active catalysts for oxygen evolution in alkaline solution, *Nat. Commun.*, 2013, 4, 2439.

56 S. Sinthika, U. V. Waghmare and R. Thapa, Structural and electronic descriptors of catalytic activity of graphene-based materials: first-principles theoretical analysis, *Small*, 2017, 14, 1703609.

57 Y. Y. Birdja, J. Shen and M. T. M. Koper, Influence of the metal center of metalloprotoporphyrins on the electrocatalytic CO_2 reduction to formic acid, *Catal. Today*, 2017, 288, 37–47.

58 N. Spataru, K. Tokuhiro, C. Terashima, T. N. Rao and A. Fujishima, Electrochemical reduction of carbon dioxide at ruthenium dioxide deposited on boron-doped diamond, *J. Appl. Electrochem.*, 2003, 33, 1205–1210.

59 P. Kang, C. Cheng, Z. Chen, C. K. Schauer, T. J. Meyer and M. Brookhart, Selective Electrocatalytic Reduction of CO_2 to Formate by Water-Stable Iridium Dihydride Pincer Complexes, *J. Am. Chem. Soc.*, 2012, 134, 5500–5503.

60 R. Kortlever, I. Peters, S. Koper and M. T. M. Koper, Electrochemical CO_2 Reduction to Formic Acid at Low Overpotential and with High Faradaic Efficiency on Carbon-Supported Bimetallic Pd–Pt Nanoparticles, *ACS Catal.*, 2015, 5, 3916–3923.

61 W. Zhang, Y. Hu, L. Ma, G. Zhu, Y. Wang, X. Xue, R. Chen, S. Yang and Z. Jin, Progress and Perspective of Electrocatalytic CO_2 Reduction for Renewable Carbonaceous Fuels and Chemicals, *Adv. Sci.*, 2018, 5, 1700275.

62 X.-L. Lu, X. Rong, C. Zhang and T.-B. Lu, Carbon-based single-atom catalysts for CO_2 electroreduction: progress and optimization strategies, *J. Mater. Chem. A*, 2020, 8, 10695–10708.

63 Q. Wang, Y. Lei, D. Wang and Y. Li, Defect engineering in earth-abundant electrocatalysts for CO_2 and N_2 reduction, *Energy Environ. Sci.*, 2019, 12, 1730–1750.

64 R. Qin, K. Liu, Q. Wu and N. Zheng, Surface Coordination Chemistry of Atomically Dispersed Metal Catalysts, *Chem. Rev.*, 2020, 120, 11810–11899.

65 C. Zhao, Y. Wang, Z. Li, W. Chen, Q. Xu, D. He, D. Xi, Q. Zhang, T. Yuan, Y. Qu, J. Yang, F. Zhou, Z. Yang, X. Wang, J. Wang, J. Luo, Y. Li, H. Duan and Y. Li, Solid-diffusion synthesis of single-atom catalysts directly from bulk metal for efficient CO_2 reduction, *Joule*, 2019, 3, 584–594.

66 P. Su, K. Iwase, S. Nakanishi, K. Hashimoto and K. Kamiya, Nickel-nitrogen-modified graphene: an efficient electrocatalyst for the reduction of carbon dioxide to carbon monoxide, *Small*, 2016, 12, 6083–6089.

67 L. Wang, J. Zhang, L. Zheng, J. Yang, Y. Li, X. Wan, X. Liu, X. Zhang, R. Yua and J. Shui, Carbon Black Supported FM-NC (FM ¼ Fe, Co, Ni) Single-Atom Catalysts Synthesized by Self-Catalysis of Oxygen Coordinated Ferrous Metal Atoms, *J. Mater. Chem. A*, 2020, 8, 13166–13172.

68 Y. Hou, Y.-B. Huang, Y.-L. Liang, G.-L. Chai, J.-D. Yi, T. Zhang, K.-T. Zang, J. Luo, R. Xu, H. Lin, S.-Y. Zhang, H.-M. Wang and R. Cao, Unraveling the Reactivity and Selectivity of Atomically Isolated Metal–Nitrogen Sites Anchored on Porphyrinic Triazine Frameworks for Electroreduction of CO_2, *CCS Chem.*, 2019, 1, 384–395.

69 Y. Wang, Z. Jiang, X. Zhang, Z. Niu, Q. Zhou, X. Wang, H. Li, Z. Lin, H. Zheng and Y. Liang, Metal Phthalocyanine-Derived Single-Atom Catalysts for Selective CO_2 Electroreduction

under High Current Densities, *ACS Appl. Mater. Interfaces*, 2020, 12, 33795–33802.

70 J.-F. Sun, J.-T. Wu, Q.-Q. Xu, D. Zhou and J.-Z. Yin, CO_2 electrochemical reduction using single-atom catalysts. Preparation, characterization and anchoring strategies: a review, *Environ. Chem. Lett.*, 2020, 18, 1593–1623.

71 X. Wang, Z. Chen, X. Zhao, T. Yao, W. Chen, R. You, C. Zhao, G. Wu, J. Wang, W. Huang, J. Yang, X. Hong, S. Wei, Y. Wu and Y. Li, Regulation of Coordination Number over Single Co Sites: Triggering the Efficient Electroreduction of CO_2, *Angew. Chem., Int. Ed.*, 2018, 57, 1944–1948.

72 T. Wang, X. Sang, W. Zheng, B. Yang, S. Yao, C. Lei, Z. Li, Q. He, J. Lu, L. Lei, L. Dai and Y. Hou, Gas Diffusion Strategy for Inserting Atomic Iron Sites into Graphitized Carbon Supports for Unusually High-Efficient CO_2 Electroreduction and High-Performance Zn–CO_2 Batteries, *Adv. Mater.*, 2020, 32, 2002430.

73 R. Daiyan, X. Zhu, Z. Tong, L. Gong, A. Razmjou, R.-S. Liu, Z. Xia, X. Lu, L. Dai and R. Amal, Transforming active sites in nickel–nitrogen–carbon catalysts for efficient electrochemical CO_2 reduction to CO, *Nano Energy*, 2020, 78, 105213.

74 M.-J. Cheng, E. L. Clark, H. H. Pham, A. T. Bell and M. Head-Gordon, Quantum Mechanical Screening of Single-Atom Bimetallic Alloys for the Selective Reduction of CO_2 to C_1 Hydrocarbons, *ACS Catal.*, 2016, 6, 7769–7777.

75 P. Hirunsit, Electroreduction of carbon dioxide to methane on copper, copper–silver, and copper–gold catalysts: a DFT study, *J. Phys. Chem. C*, 2013, 117, 8262–8268.

76 L. C. Grabow and M. Mavrikakis, Mechanism of Methanol Synthesis on Cu through CO_2 and CO Hydrogenation, *ACS Catal.*, 2011, 1, 365–384.

77 I. V. Solovyev, P. H. Dederichs and V. I. Anisimov, Corrected atomic limit in the local-density approximation and the electronic structure of d impurities in Rb, *Phys. Rev. B: Condens. Matter Mater. Phys.*, 1994, 50, 16861–16871.

78 J. P. Perdew, K. Burke and M. Ernzerhof, Generalized Gradient Approximation Made Simple, *Phys. Rev. Lett.*, 1997, 77, 3865–3868.

79 V. L. Deringer, A. L. Tchougr´eeff and R. Dronskowski, Crystal orbital Hamilton population (COHP) analysis as projected from plane-wave basis sets, *J. Phys. Chem. A*, 2011, 115, 5461–5466.

80 S. Maintz, V. L. Deringer, A. L. Tchougr´eeff and R. Dronskowski, LOBSTER: a tool to extract chemical bonding from plane-wave based DFT, *J. Comput. Chem.*, 2016, 37, 1030–1035.